Mn^{2+} defects in $LiNbO_3$: an electron nuclear double resonance (ENDOR) investigation of the Mn^{2+} site and the local disorder

1990 J. Phys.: Condens. Matter 2 6603

(http://iopscience.iop.org/0953-8984/2/31/013)

J. Phys.: Condens. Matter 2 (1990) 6603–6618. Printed in the UK

Mn^{2+} defects in $LiNbO_3$: an electron nuclear double resonance (ENDOR) investigation of the Mn^{2+} site and the local disorder

G Corradi†§, H Söthe†, J-M Spaeth† and K Polgár‡

† Fachbereich Physik, Universität Paderborn, Warburger Straße 100A, D-4790 Paderborn, Federal Republic of Germany

‡ Research Laboratory for Crystal Physics of the Hungarian Academy of Sciences, PO Box 132, H-1502 Budapest, Hungary

Received 28 March 1990

Abstract. With ENDOR, Mn^{2+} centres in both stoichiometric and congruent $LiNbO_3$ have been investigated. An analysis of four identified Li shells with 24 Li neighbours gives sufficient proof for the Mn^{2+} occupying a Li site. In stoichiometric $LiNbO_3$ both neighbouring on-axis Nb nuclei were also identified and found to experience changed electric field gradients compared with remote Nb nuclei and NMR data in the literature. Signs of the parameters of the Mn^{2+} spin Hamiltonian ($A_{\parallel,\perp} < 0$, $D > O$, $P > 0$) have been determined. Most centres probably contain a defect such as a charge-compensating Li vacancy in the first Li shell. As inferred from line-broadening effects, additional defects, especially in congruent crystals, have a measurable influence on the relaxations of nuclei near to the Mn^{2+}.

1. Introduction

The atomic configuration and electronic structure of transition metal centres in lithium niobate ($LiNbO_3$) are of basic interest owing to the strong influence of these impurities on the photorefractive effect and the practical consequences of this phenomenon (Peterson *et al* 1971, Phillips *et al* 1972, Glass 1978). For the basic Mn^{2+} centre, similarly to the case of most other transition metal dopants, only the axial position of the Mn^{2+} could be established because all positions along the c axis have the same C_3 symmetry (for an early review see Räuber 1978). A comparison of the electric field gradients as inferred from the splittings of forbidden ESR lines (Mn^{2+}) or from Mössbauer spectra (Fe^{3+}) with values obtained for the bulk by NMR favoured the Li site for Mn^{2+} and the Nb site for Fe^{3+} (Malovichko and Grachev 1985). Mn^{2+} substitution for Li^+ was also strongly supported by recent EXAFS results of Zaldo and Agulló-López (1989). An analysis of the observed temperature dependence of the local crystal-field constant D for Fe^{3+} suggested that with increasing temperature the Fe^{3+} ion moves towards the centre of its oxygen octahedron like the Nb^{5+} ions (Agulló-López and Müller 1987).

However, the situation may be complicated by the non-stoichiometric character of $LiNbO_3$ and by uncontrolled impurities. The irregularities or stacking faults in the

§ Permanent address: Research Laboratory for Crystal Physics of the Hungarian Academy of Sciences, PO Box 132, H-1502 Budapest, Hungary.

0953-8984/90/316603+16$03.50

cation sublattice, due to the large Li deficiency in congruent $LiNbO_3$ (Räuber 1978) were interpreted in terms of sections of ilmenite stacking order along the c axis (LiNb NbLi LiNb) (Smyth 1983). Accordingly, a local modification of the stacking order near the dopant ion cannot be excluded either. Impurities might cause similar effects. For example with ENDOR, Cr^{3+} was found to form associates with Al, a common impurity in $LiNbO_3$ (Grachev *et al* 1987).

Recently ENDOR has also been used to confirm sites of Fe^{3+} centres in $KTaO_3$ (Laguta *et al* 1987) and $LiTaO_3$ (Söthe *et al* 1989). This method can give direct information on the identity and the superhyperfine (SHF) and quadrupole interactions of the neighbouring nuclei except those with zero spin (e.g. ^{16}O, the only abundant oxygen isotope).

In order to clarify the local structure near the Mn^{2+} dopant in $LiNbO_3$, in this work an ENDOR study has been carried out. The results were used for unambiguous determination of the impurity site and the local stacking order of cations. Line-broadening effects have also been analysed and give additional information on the accompanying defects and the relaxations of neighbours near the Mn^{2+}.

A preliminary report on the results, showing that Mn^{2+} in $LiNbO_3$ substitutes for Li^+, has been published earlier (Corradi *et al* 1988).

2. Experimental procedures

Congruent and 'stoichiometric' $LiNbO_3$ crystals were grown in air using Merck Suprapure and Grade I Johnson Matthey materials from melts having starting Li:Nb compositions of 0.946:1 and 1.2:1 and Mn^{2+} concentrations of 10^{-2} or 2×10^{-2} mol%, respectively. A balance-controlled Czochralski growth method (Schmidt and Voszka 1981) and a poling procedure provided optical quality single-domain crystals. The high quality of the crystals was also characterised by low values (20 s^{-1}) of the spin–lattice relaxation rate at liquid-helium temperature (Corradi *et al* 1984). The ESR and stationary ENDOR experiments were performed with custom-built computer-controlled X-band spectrometers. The sample temperature could be varied between 4 and 300 K; the ENDOR frequency could be varied in the range between 0.5 and 300 MHz. The ENDOR line positions were determined using digital filtering, deconvolution algorithms and a special peak search algorithm (Niklas 1983).

3. ENDOR results for Li and Nb nuclei

The ESR spectra ($3d^5$ configuration, $S = \frac{5}{2}$, with axial symmetry along the threefold crystal c axis, and resolved hyperfine sextets due to the ^{55}Mn nucleus) were found to be the same as those reported for Mn^{2+} by Takeda *et al* (1968), Petrov (1968), Rexford and Kim (1972) and Herrington *et al* (1972). The electron g factor is 1.998 and the fine-structure splitting D is 2192 MHz (Rexford and Kim 1972). Our ENDOR investigations were confined to the vicinity of special orientations of the external magnetic field ($\boldsymbol{B}_0 \parallel \boldsymbol{c}$ and $\boldsymbol{B}_0 \perp \boldsymbol{c}$) owing to line-broadening effects, especially in the congruent case. ENDOR spectra were preferably investigated for high-field ($B_0 > 300$ mT) ESR transitions where better signal-to-noise ratios could be achieved. The ESR and ENDOR

spectra were analysed using the Hamiltonian (Seidel 1961, 1966)

$$\mathcal{H} = \mathcal{H}_{\mathrm{Mn}} + \sum_i \mathcal{H}_i \tag{1}$$

$$\mathcal{H}_{\mathrm{Mn}} = g\mu_{\mathrm{B}}\boldsymbol{B}_0 \cdot \boldsymbol{S} + D[S_z^2 - \tfrac{1}{3}S(S+1)] + A_{\parallel}S_zI_z + A_{\perp}(S_xI_x + S_yI_y) - g_{\mathrm{n}}\mu_{\mathrm{n}}\boldsymbol{B}_0 \cdot \boldsymbol{I} + P[I_z^2 - \tfrac{1}{3}I(I+1)] \tag{2}$$

$$\mathcal{H}_i = \boldsymbol{S} \cdot \tilde{\mathbf{A}}_i \cdot \boldsymbol{I}_i - g_{\mathrm{n},i}\mu_{\mathrm{n}}\boldsymbol{B}_0 \cdot \boldsymbol{I}_i + P_i[I_{iz}^2 - \tfrac{1}{3}I_i(I_i+1)] \tag{3}$$

where i stands for (neighbouring) magnetic nuclei. For Mn this index is omitted. The z and x axes are parallel to the crystal c axis and one of the three non-piezoelectric directions, respectively. The other quantities are as follows: g and $g_{\mathrm{n},i}$ are the isotropic electron and nuclear g factors, D is the axial crystal-field parameter, the $\tilde{\mathbf{A}}_i$ are SHF interaction tensors and the P_i are the quadrupole splitting constants. As found by Rexford and Kim (1972) the crystal-field parameters other than D are very small compared with the Zeeman energy and could be omitted for calculating the ENDOR frequencies. For the nuclei considered, the main principal axes of the quadrupole tensors could be assumed to be parallel to the c axis.

The ENDOR spectra consist of low-frequency lines due to Li and Nb nuclei and of lines at higher frequencies due to Mn. No lines could be attributed to other impurities. The Li and Nb lines are better resolved in stoichiometric (figure 1(a)) than in congruent $LiNbO_3$ (figure 1(b)). ENDOR lines of ^{6}Li, ^{7}Li and ^{93}Nb could be identified by applying the magnetic field dependence method (Seidel and Wolf 1968). For the prominent ^{7}Li lines ($I = \frac{3}{2}$; natural abundance, 92.6%; $g_{\mathrm{n}} = 2.1707$), quadrupole splitting is unresolved. The small sharp ^{6}Li lines ($I = 1$; natural abundance, 7.4%; $g_{\mathrm{n}} = 0.821\,92$) exactly repeat the ^{7}Li pattern scaled down according to the g_{n} values. For ^{93}Nb ($I = \frac{9}{2}$; natural abundance, 100%; $g_{\mathrm{n}} = 1.3652$), however, quadrupole nonets are observed with sharper central lines and hardly measurable broadened wing lines.

The angular dependence of the ENDOR line positions for rotation of the magnetic field from the x to the y axis (maintaining $\boldsymbol{B}_0 \perp \boldsymbol{c}$ with B_0 constant) is shown in figures 2 and 3. The ^{7}Li lines in figure 2 (measured at $B_0 = 352.5$ mT) are grouped around the Larmor frequency ν_{n} of ^{7}Li and show an angular dependence which is very similar to that found previously for the Fe^{3+} centres in $LiTaO_3$ (Söthe *et al* 1989). Immediately seen is a single 60° symmetry pattern which indicates that the Mn^{2+} must be on the symmetry axis of the crystal. In a similar way to the argument of Söthe *et al*, this line pattern implies that Mn^{2+} substitutes for Li^+ (see also below). If the Mn^{2+} substituted for Nb^{5+}, one would expect angle-independent Li lines for $\boldsymbol{B}_0 \perp \boldsymbol{c}$ (Söthe *et al* 1989). In figure 2 no such 'isotropic' Li line could be resolved, i.e. all observed Li shells are off the c axis.

On the other hand, the Nb ENDOR transitions (figure 3, measured at a higher magnetic field $B_0 = 513.9$ mT) do show many angle-independent lines for $\boldsymbol{B}_0 \perp \boldsymbol{c}$, which imply the presence of nearby Nb ions on the C_3 centre axis (see also figure 4). In fact the Nb ions on the C_3 axis have axially symmetric SHF and quadrupole tensors with their main principal axes along the C_3 axis; consequently in the plane perpendicular to the C_3 axis the ENDOR lines are not angle dependent. The same arguments show that no Li nuclei were found on the symmetry axis, implying that the nearby Mn^{2+} are on a substitutional Li site.

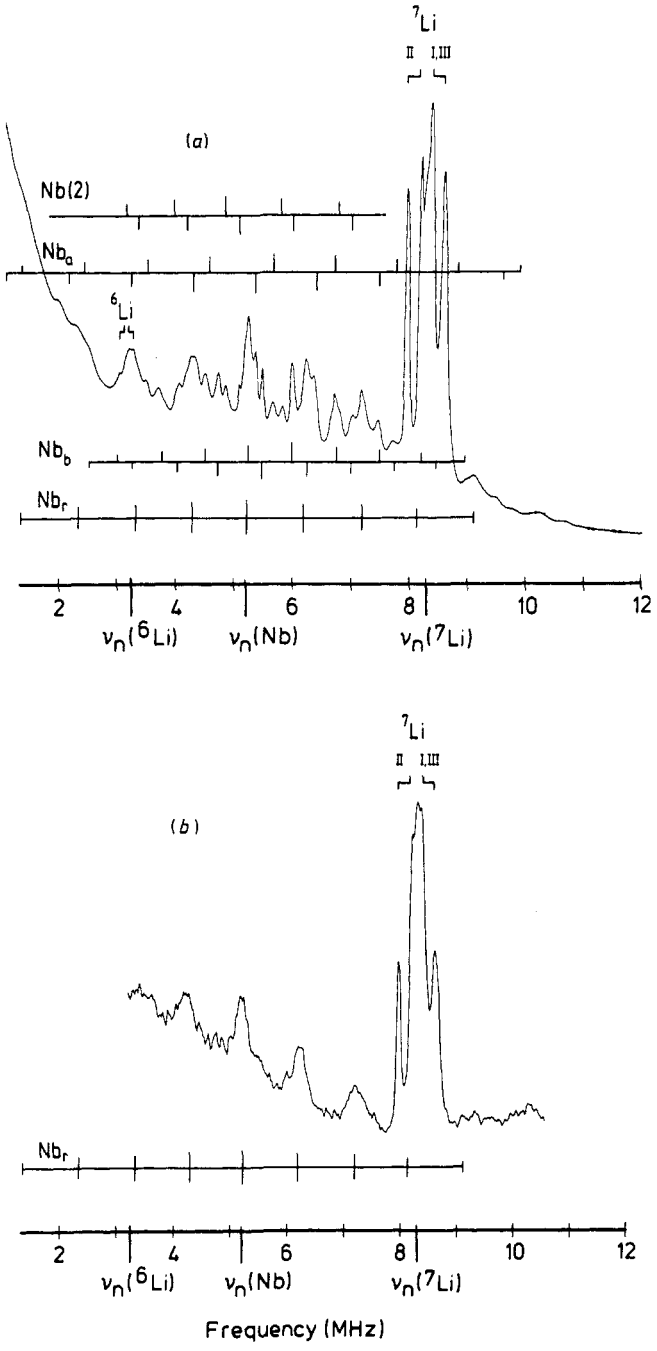

Figure 1. (*a*) Part of the ENDOR spectrum of Mn^{2+} centres in stoichiometric $LiNbO_3$ for $\boldsymbol{B}_0 \parallel \mathbf{c}$ (B_0 = 500.4 mT) at $T \simeq 8$ K for the $m_s = -\frac{1}{2} \longleftrightarrow m_s = -\frac{3}{2}$ ESR transition. The lines corresponding to the nearest Li shells, the on-axis Nb_a and Nb_b neighbours, remote Nb nuclei and an off-axis Nb shell (2) are indicated. Vertical bars are used for the ENDOR transitions for $m_s = -\frac{3}{2}$ (up) and $m_s = -\frac{1}{2}$ (down), respectively. (*b*) Same spectrum as in (*a*) for a congruent crystal. Only the nearest ^{7}Li shells and remote Nb nuclei yield resolved ENDOR lines.

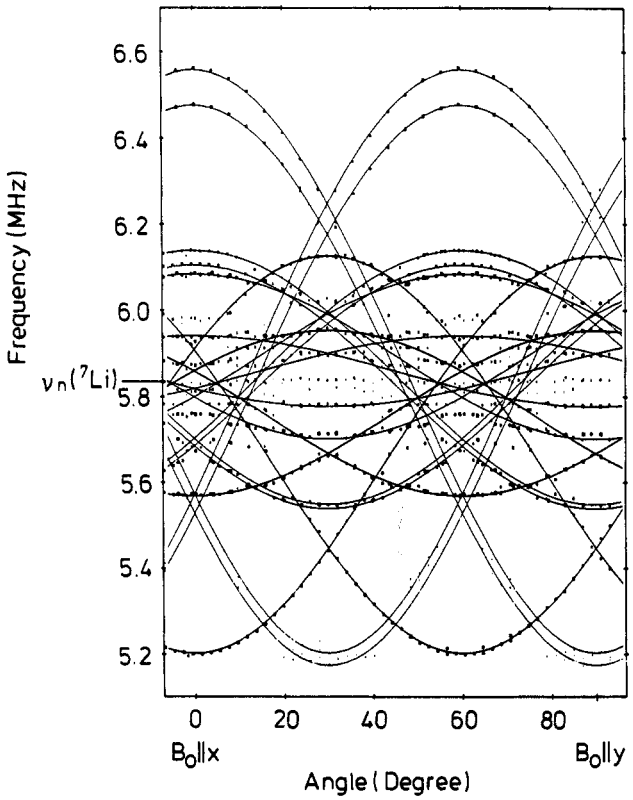

Figure 2. Angular dependence of ^{7}Li ENDOR line positions in stoichiometric $LiNbO_3$:Mn^{2+} for the $m_{s\,\mathrm{eff}} = 0.57 \longleftrightarrow m_{s\,\mathrm{eff}} = 1.36$ ESR transition for the magnetic field $\boldsymbol{B}_0$ rotating in the plane perpendicular to the c axis ($B_0 = 352.5$ mT). The sizes of the points indicate the peak heights; the curves are the calculated angular dependences with the interaction constants in table 1.

The ENDOR frequencies were analysed in the effective-spin approximation (Seidel 1961, 1966). The spin Hamiltonian (1)–(3) can be diagonalised in two steps. First the electron Zeeman term and the crystal-field term are diagonalised numerically. The effective spin quantum number $m_{s\,\mathrm{eff}}$ is calculated as the component of the expectation value $\langle \boldsymbol{S}_z \rangle$ parallel to $\boldsymbol{B}_0$. For $\boldsymbol{B}_0 \parallel \boldsymbol{c}$, $m_{s\,\mathrm{eff}} = m_s$. The value of $m_{s\,\mathrm{eff}}$ depends on the fine-structure constant D and the magnetic field $\boldsymbol{B}_0$ where the ENDOR transition was measured. In this approximation the hyperfine constant can be neglected. The calculated $m_{s\,\mathrm{eff}}$ differ by about 0.1 from those of m_s (see table 2). This $m_{s\,\mathrm{eff}}$ is introduced in the nuclear spin Hamiltonian (equation (3)), which is then diagonalised within the nuclear quantum states.

The ENDOR frequency for the $m_{I,i} \rightarrow m_{I,i} + 1$ spin transition of nucleus i, to first order in the SHF and quadrupole energies, is of the form

$$\nu_i \simeq |\nu_{\mathrm{n},i} - m_{s\,\mathrm{eff}}(D)A_i(\vartheta_i, \psi_i, \varphi_i, \Theta) - (m_{I,i} + \tfrac{1}{2})p_i(\Theta)| \tag{4}$$

where $\nu_{\mathrm{n},i} = g_{\mathrm{n},i}\mu_{\mathrm{n}}B_0/h$ are the nuclear Larmor frequencies, and A_i and p_i are orientation dependent SHF and quadrupole interaction energies divided by h. The Euler angles ϑ_i, ψ_i and φ_i define the principal directions of the SHF tensors with respect to

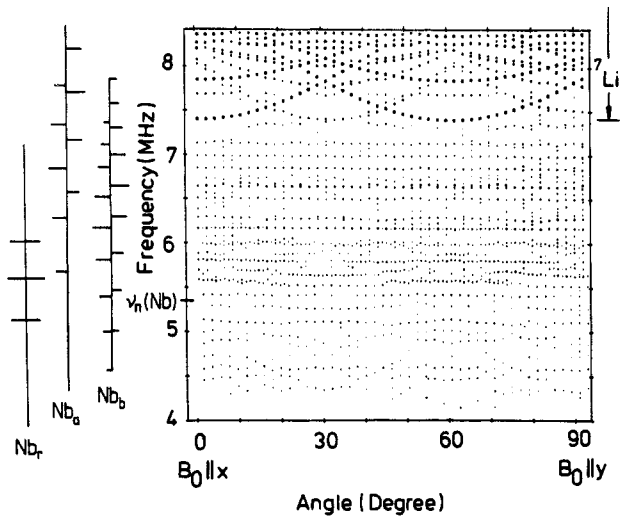

Figure 3. Angular dependence of the ^{93}Nb ENDOR line positions in stoichiometric $LiNbO_3$ for the $m_{s\,\mathrm{eff}} = 1.40$ (bars left) $\longleftrightarrow$ $m_{s\,\mathrm{eff}} = 2.39$ (bars right) ESR transition for the magnetic field $\boldsymbol{B}_0$ rotating perpendicular to the c axis ($B_0 = 513.9$ mT). The ENDOR lines above 7 MHz are due to ^{7}Li and are identical with those shown in figure 2 when measuring in another Mn ESR transition at a lower field.

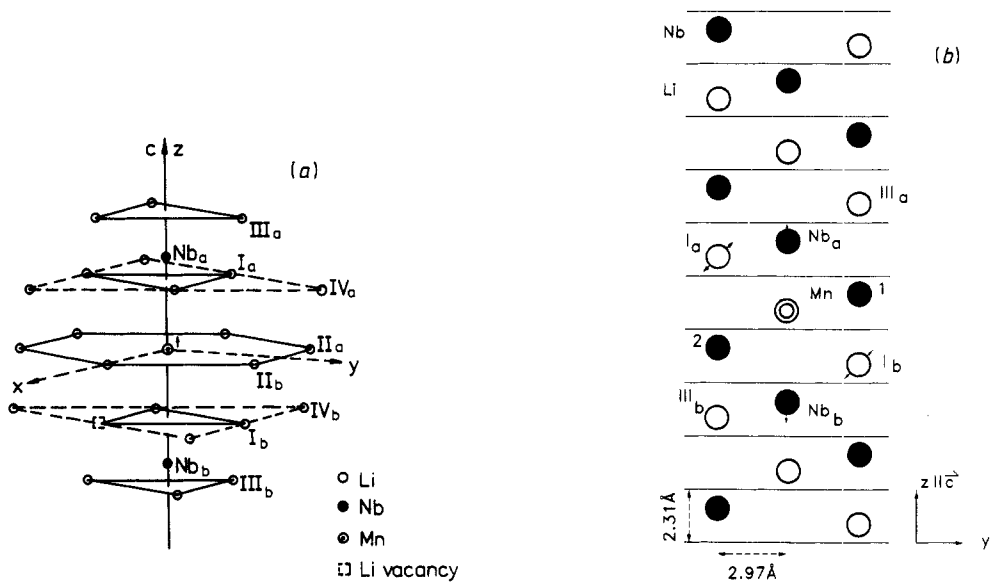

Figure 4. (*a*) Identified Li shells and on-axis $Nb_{a,b}$ nuclei assuming that Mn^{2+} substitutes for Li^+. The tentatively identified off-axis Nb shell is omitted. A Li vacancy presumably present in the I_b subshell is indicated. (*b*) Nuclei in the y–z plane in the centre model. The arrows indicate characteristic displacements of some neighbours. The horizontal lines indicate oxygen planes.

the crystal axes, while Θ stands for the direction of the magnetic field. For example, for $\boldsymbol{B}_0 \perp \boldsymbol{c}$, Θ is the angle between the magnetic field and the x axis.

Table 1. Experimental values for SHF and quadrupole constants (in MHz) for cation shells around the Mn^{2+} centre in stoichiometric $LiNbO_3$. Values of the isotropic constant a and anisotropic SHF constants b, b' and Euler angles $\vartheta, \psi(=0°), \varphi$ specifying the principal SHF directions, or only the SHF splitting $A_{\|}$ at $\boldsymbol{B}_0 \parallel \boldsymbol{c}$ are given. NMR–NQR data for the quadrupole coupling constant eqQ are included for comparison. Some results of point-dipole calculations for both cation sites in the $LiNbO_3$ lattice and for the structural vacancy in an ilmenite lattice are also included, where $r, \vartheta, \varphi + 90°$ are calculated as the usual polar coordinates of the nuclei with respect to the Mn^{2+} position and the coordinate axes given in figure 4(*a*). Experimental errors are estimated to be less than one or two units of the last digit given; for numbers followed by a †, errors may be larger by a factor of 5.

	^{7}Li shells					^{93}Nb shells				
Shell	I_a	I_b	$II_{a,b}$	$III_{a,b}$	$IV_{a,b}$	Nb_a	Nb_b	Off-axis shell 1	Off-axis shell 2	Remote shells
No of nuclei	3	3	6	6	6	1	1	3	3	
ENDOR experiment										
$A_{\|}$									−0.22	0 ± 0.1
a	0.06	0.08	0.01	0.05	−0.01	−0.50	−0.16			
$b - b'$	0.59	0.55	0.227	0.24	0.09	0.40	0.34			
b'	−0.08†	−0.08†	0.00	−0.07†		0.00	0.00			
ϑ	53°	53°	90°	36°	69°†	0°	0°			
φ	0°	±1.5°	30°	0°	0°	—	—		0°	
$\|eqQ\|$			$\lesssim$ 0.08[a]			25	17.8		22	23
Calculated for Mn^{2+} on										
Li site										
r (Å)		3.766		5.151	5.496	6.381	3.063	3.870	3.067	3.357
b		0.57		0.225	0.19	0.12	0.67	0.33	0.67	0.51
ϑ		52°		90°	33°	69°	0°	0°	76°	62°
Nb site										
b	1.07	0.81		0.13	0.14	0.11				
ϑ	76°	62°		56°	79°	27°				
Ilmenite V site										
b		0.45		0.19	0.11	0.09				
ϑ		47°		70°	65°	25°				
Literature, NMR										
$\|eqQ\|$					0.055[b]					23.6[c]

[a] Estimate from linewidth, see table 2.
[b] Peterson *et al* (1967).
[c] Schempp *et al* (1970), value for 20 K.

In table 1 the SHF interactions are given in terms of the isotropic SHF constants a and the anisotropic SHF constants b and b' related to the three principal values of the SHF tensors by $A_{xx} = a - b + b'$, $A_{yy} = a - b - b'$ and $A_{zz} = a + 2b$. The quadrupole data are given in terms of the quadrupole coupling constant $eqQ = 4I(2I-1)P/3$, where $q = \partial^2 V_{zz}/\partial z^2$ is the electric field gradient seen by the nucleus and Q is the quadrupole moment of the nucleus.

For the first ^{7}Li shell, two weakly inequivalent subshells (I_a and I_b) were found. The dipole–dipole SHF interaction with strong axial character clearly dominates the isotropic interaction for all Li shells and to a lesser extent for Nb_b. For the Li shell

$II_{a,b}$ the SHF interaction was found to be axial within experimental error along x-type directions. In addition to $b \gg |a|, |b'|$, the prediction of the classical point-dipole–dipole approximation,

$$b_i = g\mu_B g_{n,i}\mu_n r^{-3} \tag{5}$$

explains the experimental b values for all Li shells and the Nb_b shell if the Li site is assumed for Mn^{2+} (see table 1 where other substitutional sites are also considered). In this approximation, ψ is undefined and r, ϑ and $\varphi + 90°$ are the usual polar coordinates of the ligand nucleus with respect to the Mn^{2+} position. All other positions along the c axis can be excluded as seen from figure 5. In this figure the distances of Li shells are calculated as a function of the displacement of the Mn^{2+} from the Li site. No explanation of the data could be achieved for any site in the ilmenite structure. The Li site is also in agreement with the symmetry of the ENDOR angular dependence discussed above. Very similar results were found for Fe^{3+} centres in $LiTaO_3$ (Söthe *et al* 1989).

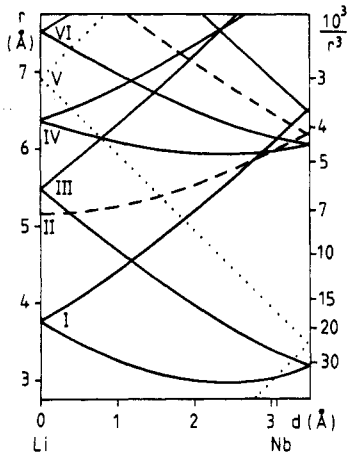

Figure 5. Distances of Li shells as a function of the displacement d of the Mn^{2+} ion along the c axis in the $LiNbO_3$ lattice, $d = 0$ corresponding to Li^+ substitution. Li shells with $\varphi = 0°$, $\varphi = 30°$ and $\vartheta = 0°$ are represented by full, broken and dotted curves respectively. The r^{-3} axis is included for comparisons based on the point-dipole model ($b \sim r^{-3}$).

As in the case of Fe^{3+} the $3d^5$ orbitals apparently have very little overlap transfer via the oxygen neighbours to the Li shells, resulting in very small isotropic SHF interactions. Only for the first Nb shell (Nb_a) does the classical dipole–dipole interaction not explain the measured b value. Only this shell has an appreciable isotropic constant ($|a| > |b|$) with a negative sign. The anisotropic constant b was found to be positive from experimental data. The fact that a and b have opposite signs and that b is smaller than the classical dipole–dipole interaction points to a large contribution of spin polarisation (Adrian *et al* 1985). Probably this spin polarisation is caused by intermediate oxygen ions. The assignment of this shell is, however, unambiguous from the symmetry.

For an off-axis Nb shell (see Nb(2) in figure 1(a)), because of lack of resolution at $\boldsymbol{B}_0 \perp \boldsymbol{c}$, only the values of the splitting constants $A_{\|}$ and P could be determined, the latter on the assumption that even for this shell the main principal axis of the field gradient tensor is closely parallel to the c axis. This assumption was checked by estimating the angle between the mentioned principal axis and the c axis from the observed small higher-order negative quadrupole shift (−0.04 MHz) of the central

transitions of the respective nonets at $\boldsymbol{B}_0 \parallel \boldsymbol{c}$ (Cohen and Reif 1959, Peterson and Bridenbaugh 1968) and a deviation of only about 8° was found. This Nb shell can be tentatively identified with the second off-axis Nb shell denoted 2 in figure 4(*b*).

A nonet of broad SHF lines with very small SHF interactions at $\boldsymbol{B}_0 \parallel \boldsymbol{c}$ can be attributed to remote Nb shells, including also the third-nearest off-axis Nb shell (r = 5.96 Å, $\vartheta \simeq 60°$, $\varphi \simeq 30°$). Some features corresponding to these shells are also seen for $\boldsymbol{B}_0 \perp \boldsymbol{c}$. ENDOR lines of the first off-axis Nb shell could not be identified (see section 5).

The observed off-axis shells are of two easily discernible types: $\varphi \simeq 0°$ for nuclei in y–z-type planes and $\varphi \simeq 30°$ for nuclei in x–z-type planes. The assumption $\psi = \varphi = 0°$ fixing one of the principal SHF axes parallel to the x axis was inevitable for $\varphi \simeq 0°$ shells, since in $LiNbO_3$ there are two inequivalent Li (or any other on-axis) sites with different orientations of the oxygen octahedra around them. The two kinds of site are connected by y–z-type glide planes. This should lead to different signs of ψ and φ for the two kinds and might lead to broadening or splitting of the ENDOR lines for general orientations of $\boldsymbol{B}_0$ outside the y–z plane. This effect should be very similar for both subshells of a given shell. In contrast with this another effect of the same type of symmetry but only for subshell I_b and not for I_a has been observed.

As shown in figure 6, in stoichiometric $LiNbO_3$ for $m_{s\,\mathrm{eff}} = 2.39$ a splitting at $\Theta = 24°$ can be observed for subshell I_b and may correspond to deviations of the order of $\psi = 10°$ and/or $\varphi = 1°$. However, for subshell I_a in stoichiometric $LiNbO_3$ no broadening was observed for at least up to $\Theta = 30°$. A straightforward explanation of the different behaviour may be a Li vacancy in the I_b subshell for most of the centres. The two components of the doublet splitting may then correspond to the two remaining sites of the vacancy within the subshell (besides the Li nucleus giving the ENDOR transition). Again the possible vacancy positions are symmetric with respect to the y–z plane, i.e. no similar splitting for $\boldsymbol{B}_0 \parallel \boldsymbol{x}$ and $\boldsymbol{B}_0 \parallel \boldsymbol{y}$ is expected. (For broadening at $\boldsymbol{B}_0 \parallel \boldsymbol{y}$ see section 5). If only a deviation of φ from zero is considered, values as small as $\varphi = \pm 1.5°$ are sufficient to explain the observed doublet splitting. This may correspond to a relaxation within the incomplete subshell. A vacancy in the I_b subshell could well be the reason for the inequivalence of the first subshells, since the subshell I_a on the other side of the x–y plane would be less affected.

In order to see whether Mn^{2+} precisely substitutes for Li^+ a small deviation of the Mn^{2+} position along the c axis was considered. If the slight difference between the b values of subshells $I_{a,b}$ was attributed to a small displacement d of Mn, $|d| \simeq 0.07$ Å would result. However, an estimate of $|d|$. 0.04 Å arises from the fact that the lines of shell $III_{a,b}$ are unsplit (see below). The latter estimate should be given more credit since shell $III_{a,b}$ is less perturbed and the point-dipole approximation is also better for this shell. A small displacement of Mn^{2+} seems likely to be an additional cause for the inequivalence of subshells I_a and I_b (see also below). Note that the measurements were done in the ferroelectric phase.

The position of the Mn is firmly established with respect to the off-axis Li ions of the $LiNbO_3$ lattice, without reference to the stacking sequence along the centre axis, which might in principle be modified or weakly defined. The absence of an on-axis Li neighbour within 6 Å (as estimated from the point-dipole approximation) and the presence of two close on-axis Nb neighbours in stoichiometric $LiNbO_3$ with Nb_a clearly nearer than Nb_b gives additional, decisive proof for Li substitution and discards, at least in stoichiometric $LiNbO_3$, the possibility of a locally modified stacking sequence

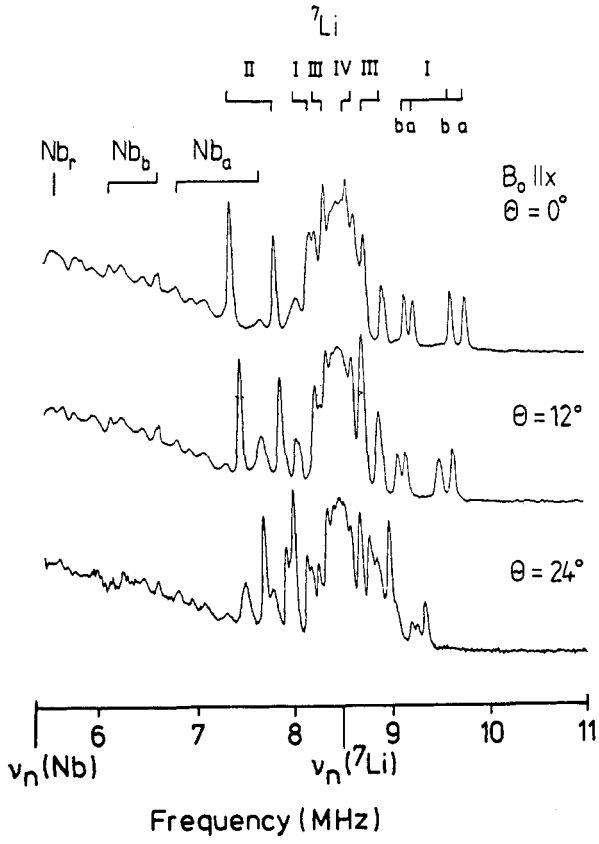

Figure 6. Part of the ENDOR spectrum at $T \simeq 11$ K in the stoichiometric case for the $m_{s\,\mathrm{eff}} = 1.40$ (bars down) $\longleftrightarrow$ $m_{s\,\mathrm{eff}} = 2.39$ (bars up) ESR transition for three $\boldsymbol{B}_0 \perp \boldsymbol{c}$ orientations ($B_0 = 513.9$ mT). Note broadening and splitting for ^{7}Li subshell $\mathrm{I_b}$.

along the centre axis.

The values of the Nb quadrupole coupling constants in table 1 give new information on the electric field gradients at the Nb sites. For Nb ions in the remote and the second off-axis shells the agreement with NMR data (bulk Nb) is perfect. There is, however, an important effect for $\mathrm{Nb_{a,b}}$. The larger (smaller) quadrupole coupling constant (25 and 17.8 MHz instead of 23 MHz) indicates a larger (smaller) field gradient. This can be understood as the result of displacements in the $+c$ and $-c$ directions of $\mathrm{Nb_a}$ and $\mathrm{Nb_b}$, respectively. However, also the value of 17.8 MHz is large compared with the near-zero quadrupole coupling constant found by Peterson and Carnevale (1972) for 6% of the Nb ions sitting at irregular sites in congruent $\mathrm{LiNbO_3}$. This indicates a smaller change in the Nb position in our case, i.e. a relaxation inside the respective oxygen octahedron.

4. ENDOR results for the Mn nucleus

Mn ENDOR was expected and found at higher frequencies as shown in figure 7. The quintet splitting and the selection rules observed within the quintet unambiguously

identify the ^{55}Mn nucleus ($I = \frac{5}{2}$; natural abundance, 100%; $g_n = 1.378$). In fact, the Mn hyperfine interaction is resolved in ESR and saturation of a hyperfine component changes the population of just one m_I state which is directly involved in only one or two out of the five resolved $\Delta m_I = 1$ ENDOR transitions. The remaining lines of the quintet may still be seen because of small overlap or spin-relaxation effects with $\Delta m_I \neq 0$.

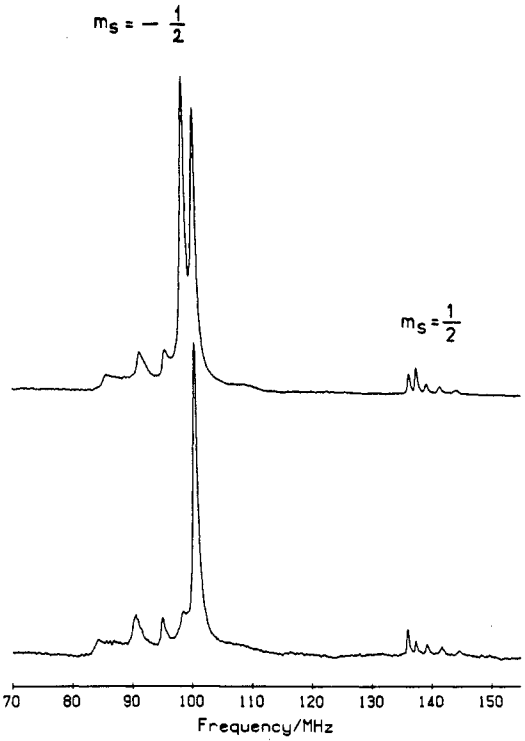

Figure 7. Mn ENDOR in stoichiometric $LiNbO_3$ for $\boldsymbol{B}_0 \parallel \boldsymbol{c}$ at $T \simeq 6$ K. The first ($m_I = -\frac{5}{2}$; $B_0 = 492.1$ mT) (lower spectrum) and second ($m_I = -\frac{3}{2}$, $\boldsymbol{B}_0 =$ 500.4 mT) (upper spectrum) hyperfine lines of the $m_s = -\frac{1}{2} \longleftrightarrow m_s = -\frac{3}{2}$ ESR transition have been saturated. The 'quadrupole' quintet for $m_s = \frac{1}{2}$ is due to indirect saturation.

Neglecting non-equidistant and asymmetric tails the spectra can be analysed using an expression accounting for the hyperfine interaction to second order (Terhune *et al* 1961). For the frequency of the $m_I \leftrightarrow m_I + 1$ transition at $\boldsymbol{B}_0 \parallel \boldsymbol{c}$ one has

$$\nu_{\parallel} = A_{\parallel} m_s - \nu_n(Mn) - K - L + (2m_I + 1)(P + K - L) \tag{6}$$

where the second-order terms are

$$K = \frac{A_{\perp}^2}{4} \frac{S(S+1) - m_s(m_s+1)}{g\mu_B B_0 + D(2m_s+1)} \tag{7}$$

$$L = \frac{A_{\perp}^2}{4} \frac{S(S+1) - m_s(m_s-1)}{g\mu_B B_0 + D(2m_s-1)}. \tag{8}$$

Using equations (6)–(8) the main quintet in figure 7 can be attributed to $m_s = -\frac{1}{2}$. The other electron spin state directly affected by the applied saturation ($m_s = -\frac{3}{2}$) is expected to yield ENDOR transitions beyond the available frequency range. The additional quintet near 140 MHz can be explained for $m_s = \frac{1}{2}$. This is a proof that the population of the $m_s = \frac{1}{2}$ multiplet is also changed by the saturation of the $m_s = -\frac{1}{2} \leftrightarrow m_s = -\frac{3}{2}$ ESR transition. The 'indirect saturation' can be due to relaxational transitions preferably with $\Delta m_s = 1$, $\Delta m_I = 0$ (see e.g. Abragam and Bleaney 1970). However, forbidden transitions with $\Delta m_s = 1$, $\Delta m_I \neq 0$ are again very important as observed also in ESR.

The results allow the determination of the signs of all constants involved: $A_{\parallel,\perp} < 0$, $D > 0$, $P > 0$, and confirm the hyperfine data of Takeda *et al* (1968), yielding $A_\parallel = -240.6 \pm 2$ MHz and $A_\perp = -231 \pm 6$ MHz, and give the value $eqQ = 16 \pm 6$ MHz for the ^{55}Mn quadrupole coupling constant. The latter value is in agreement with the result 15 ± 3 MHz (with the positive sign) of Malovichko and Grachev (1985) obtained from the splitting of forbidden ESR transitions and based on a similar second-order expression. It should be noted that the second-order hyperfine terms K and L are of the order of 10 MHz and their contribution to the splitting parameter is approximately three times larger than that of the quadrupole interaction.

For $\boldsymbol{B}_0 \perp \boldsymbol{c}$ the relative intensity of Mn^{2+} ENDOR lines due to indirect (with respect to direct) saturation was still higher. For these orientations, especially in congruent $LiNbO_3$, some additional weak ENDOR lines in the same frequency region have also been detected. These lines may belong to (strongly) perturbed Mn^{2+} centres. The existence of such centres has also been assumed by Malovichko *et al* (1986) to explain some weak additional ESR lines seen in the Q band for $\boldsymbol{B}_0 \parallel \boldsymbol{c}$. More weakly perturbed centres may be assumed to contribute, via a dominantly quadrupolar effect, only to the lineshapes of the main Mn ENDOR lines. According to Kurz *et al* (1977), perturbed transition-metal centres with low symmetry play an important role in the photorefractive effect. As discussed in the next section, perturbed Mn^{2+} centres also cause characteristic effects in ligand ENDOR.

5. Analysis of the linewidth in ligand ENDOR

A comparison of the ENDOR spectra shown in figures 1(*a*) and 1(*b*) shows that all ENDOR lines are broader in the congruent crystal. The lines of the ^{7}Li subshells I_a and I_b are broader (and not resolved) near $\boldsymbol{B}_0 \parallel \boldsymbol{y}$ than near $\boldsymbol{B}_0 \parallel \boldsymbol{x}$, even in the stoichiometric crystal. This tendency is much stronger for congruent $LiNbO_3$, where these lines tend to disappear near $\boldsymbol{B}_0 \parallel \boldsymbol{y}$. In the congruent case the rest of the ^{7}Li lines are also broadened to varying extents; the Nb lines are broadened beyond recognition with the exception of those of the remote shells at $\boldsymbol{B}_0 \parallel \boldsymbol{c}$. The ^{6}Li lines are not measurable (see figure 1(*b*)). The positions of the lines still seen are unchanged within experimental error with respect to the stoichiometric case. Experimental linewidths are collected in table 2.

The ENDOR linewidth is in principle given by the electron transverse spin relaxation time T_2 and should be the same for all ENDOR lines in one defect. However, the linewidth can also be influenced by other mechanisms. In the case of Mn^{2+} centres in $LiNbO_3$ it can be caused by

(i) unresolved and/or non-uniform quadrupole splitting due to a distribution of the electric field gradients caused by disorder,

Table 2. Linewidths (full width at half maximum) of ENDOR lines observed at $T \simeq 10$ K in $LiNbO_3$:Mn^{2+} with a precision of ±5 kHz. In the case of Nb, data are given for the $m_I = -\frac{1}{2} \longleftrightarrow m_I = \frac{1}{2}$ (central) transition. Values of the effective electron spin projections along $\boldsymbol{B}_0$ refer to a microwave frequency of about 9.0 GHz. The $m_{s\,\mathrm{eff}}$ and m_s values refer to $\boldsymbol{B}_0 \perp \boldsymbol{c}$ and $\boldsymbol{B}_0 \parallel \boldsymbol{c}$, respectively. NMR linewidth data are shown for comparison.

	Linewidth (kHz)									
	Stoichiometric					Congruent				
Shell	$\boldsymbol{B}_0 \parallel \boldsymbol{x}$	$\boldsymbol{B}_0 \parallel \boldsymbol{y}$	$(m_{s\,\mathrm{eff}})$	$\boldsymbol{B}_0 \parallel \boldsymbol{c}$	(m_s)	$\boldsymbol{B}_0 \parallel \boldsymbol{x}$	$\boldsymbol{B}_0 \parallel \boldsymbol{y}$	$(m_{s\,\mathrm{eff}})$	$\boldsymbol{B}_0 \parallel \boldsymbol{c}$	(m_s)
ENDOR										
^{7}Li, I_a	48					54				
^{7}Li, I_b	43					47				
^{7}Li, $I_{a,b}$		60	(0.57)				$\simeq 100$	(0.57)		
		70	(0.65)							
		90	(1.40)	<150	$(-\frac{3}{2})$		$\gtrsim 250$	(1.36)		
		130	(2.39)							
^{7}Li, $II_{a,b}$	45	45		80		57	57		100	
^{6}Li, $II_{a,b}$	$\simeq 25$		(1.36)							
^{7}Li, $III_{a,b}$	$\lesssim 53$	$\simeq 50$	(1.36)	<150	$(-\frac{3}{2})$	$\lesssim 70$	$\simeq 70$	(1.36)	<160	$(-\frac{3}{2})$
	70		(2.39)							
$^{93}Nb_a$	80	80	(2.39)	100	$(-\frac{3}{2})$					
$^{93}Nb_b$	50	50	(1.36)	70	$(-\frac{3}{2})$					
		$\simeq 65$	(2.39)	46	$(-\frac{1}{2})$					
^{55}Mn				890	$(-\frac{1}{2})$					
NMR										
^{7}Li									11[a]	
^{93}Nb						17[b]	17[b]		5[b]	

[a] Peterson *et al* (1967).
[b] Peterson and Carnevale (1972).

(ii) distributions of the SHF constants a, b, b' and of the SHF tensor orientations ϑ, ψ and φ due to disorder and also to the existence of slightly different subshells and inequivalent lattice sites. (This mechanism depends, in contrast with the previous one, on $m_{s\,\mathrm{eff}}$ appearing as a factor in equation (4).)

(iii) A distribution of $m_{s\,\mathrm{eff}}$ via the fine-structure constant D due to disorder.

Mechanism (iii), playing a most important role in ESR line broadening, is estimated to be unimportant, since the whole departure of $m_{s\,\mathrm{eff}}$ from m_s is about 0.1 and its variations must be clearly smaller.

For the ^{7}Li shell $II_{a,b}$ the constant linewidth for all $\boldsymbol{B}_0 \perp \boldsymbol{c}$ orientations and the nearly doubled width for $\boldsymbol{B}_0 \parallel \boldsymbol{c}$ can be approximately explained by an unresolved quadrupole splitting of a size which was observed in NMR. The relaxational width of the Li ENDOR lines can be estimated from the ^{6}Li linewidth which is smaller by a factor of 2 than that for ^{7}Li (see table 2). Since the quadrupole moment of ^{6}Li is 60 times smaller than that of ^{7}Li, quadrupole broadening seems to be important for the second and higher ^{7}Li shells.

For the first ^{7}Li shells $I_{a,b}$, quadrupole broadening is overruled at some point of the

angular dependence from $\boldsymbol{B}_0 \parallel \boldsymbol{x}$ to $\boldsymbol{B}_0 \parallel \boldsymbol{y}$ by the SHF mechanism, for the congruent crystal broadening starts nearly immediately at $\boldsymbol{B}_0 \parallel \boldsymbol{x}$. In the stoichiometric case up to at least $\Theta = 30°$, only the broadening and splitting of the I_b lines is seen, which was attributed in section 3 to mechanisms not effective at $\boldsymbol{B}_0 \parallel \boldsymbol{y}$. The broadening near $\boldsymbol{B}_0 \parallel \boldsymbol{y}$ can be best described in terms of a variation in the values of the polar angle ϑ characterising the direction of the main SHF principal axis, since the principal value $A_{xx} = a - b + b'$ directly measured at $\boldsymbol{B}_0 \parallel \boldsymbol{x}$ remains very well defined. In fact, an angle variation characterised by $\Delta\vartheta \simeq \pm 0.5°$ and $\Delta\vartheta \simeq \pm 2°$ may explain the observed broadening effects near $\boldsymbol{B}_0 \parallel \boldsymbol{y}$ in the (nearly) stoichiometric and the congruent cases, respectively. This effect may also be different for the subshells $I_{a,b}$. Apparently, some defects in or close to the first ligand shells modify the SHF interaction of the Li nuclei. Small displacements of the Mn^{2+} may also be involved, but, at least in stoichiometric $LiNbO_3$, the various broadening and splitting effects cannot be explained by a relaxation of the Mn^{2+} alone. As suggested by the well defined A_{xx} values for the subshells I_a and I_b, there seem to be only torsional relaxations in these subshells, leaving the Mn–Li distances constant but slightly different for each subshell. The observations in the stoichiometric case are consistent with the assumption that for most of the Mn^{2+} centres a charge-compensating Li vacancy is present in the first Li shell. The stronger perturbations observed for congruent $LiNbO_3$ (seen also in Mn ENDOR) may then be due to additional defects, e.g. stacking faults. The fact that in both the stoichiometric and the congruent crystals the smallest ^{7}Li linewidth has been observed for the I_b subshell at $\boldsymbol{B}_0 \parallel \boldsymbol{x}$ (see table 2) is another indication that the perturbing defect replaces a Li in this subshell. In fact, for the lines of intact subshells there are contributions from three orientations of the defect (neglecting the orientational freedom of the oxygen octahedra). These contributions never coincide exactly, while for an incomplete I_b subshell one has only two contributions coinciding at $\boldsymbol{B}_0 \parallel \boldsymbol{x}$.

Most of the broadening observed for the shells $III_{a,b}$ may be attributed to the unresolved splitting of two subshells a and b together with a quadrupolar contribution. The increased linewidth in the congruent case yields an estimate $|d|$. 0.09 Å for the average displacement of the Mn. This is only twice the limit found for the stoichiometric crystal. Consequently, also in the congruent case the Mn position is fairly well defined and close to the Li site.

The observed linewidths for the central lines of the Nb_a and Nb_b nonets at $\boldsymbol{B}_0 \parallel \boldsymbol{c}$ in the stoichiometric case give a limit of the order of ± 0.03 Å for the variations in the respective Mn–Nb distances as estimated by the point-dipole interaction. An increase in these variations by a factor of approximately 5 can explain the large line broadening observed in the congruent case. Compared with the ferroelectric Nb displacement of 0.27 Å these are still moderate variations and may also be due to the same vacancies and other defects in the nearest shells as the relaxations of the first Li shell.

The fact that we did not observe the first off-axis Nb(1) shell may be due to a strong broadening as a consequence of a SHF interaction variation. The remote Nb shells are less sensitive to disorder for $\boldsymbol{B}_0 \parallel \boldsymbol{c}$ because of their vanishing SHF interactions.

6. Conclusion

We have shown that Mn^{2+} substitutes in both stoichiometric and congruent $LiNbO_3$ for a Li^+ ion. In stoichiometric $LiNbO_3$, Mn^{2+} is probably displaced on the c axis

slightly with an upper limit of 0.04 Å. In congruent $LiNbO_3$ the displacement is less than 0.1 Å. From the analysis of the ENDOR line splitting and broadening effects it was concluded that most centres contain a defect such as a charge-compensating Li vacancy in the first shell of Li neighbours. The defects cause torsional rather than radial displacements in the first Li shell. Also the axial Nb neighbours experience slight displacements. In congruent $LiNbO_3$ the ENDOR linewidths are generally broader, which indicates more disorder compared with the stoichiometric $LiNbO_3$. The classical point dipole–dipole approximation for the anisotropic superhyperfine interaction is found to work remarkably well for all ligand shells except for the nearest Nb shells at approximately 3 Å distance from the Mn^{2+}.

Acknowledgments

This work was supported by the joint project of the Deutsche Forschungsgemeinschaft (436 UNG-113) and the Hungarian Academy of Sciences, and also by the National Scientific and Research Fund (OTKA) of Hungary. The discussions with Professor Schirmer and Professor Krätzig and with other participants of an SFB 225 seminar in Osnabrück and the friendly help of N Meilwes and Dr J Michel are greatly appreciated.

References

Abragam A and Bleaney B 1970 *Electron Paramagnetic Resonance of Transition Ions* (Oxford: Clarendon)

Adrian F J, Jette A N and Spaeth J-M 1985 *Phys. Rev.* B **31** 3923

Agulló-López F and Müller K A 1987 *Cryst. Latt. Def. Amorph. Mater.* **15** 89–95

Cohen M H and Reif F 1959 *Solid State Physics* vol 5, ed F Seitz and D Turnbull (New York: Academic) p 321

Corradi G, Polgár K, Vikhnin V S, Dovchenko L G and Zaritskii I M 1984 *Fiz. Tverd. Tela* **26** 252 (Engl. Transl. 1984 *Sov. Phys.-Solid State* **26** 149)

Corradi G, Söthe H, Spaeth J-M and Polgár K 1988 *Int. Conf. on Defects in Insulating Crystals (Parma)* Abstract TH-P25 (Parma: University of Parma)

Glass A M 1978 *Opt. Eng.* **17** 470

Grachev V G, Malovichko G I and Troitskii V V 1987 *Fiz. Tverd. Tela* **29** 607 (Engl. Transl. 1987 *Sov. Phys.-Solid State* **29** 349)

Herrington J B, Dischler B and Schneider J 1972 *Solid State Commun.* **10** 509

Kurz H, Krätzig E, Keune W, Engelmann H, Gonser U, Dischler B and Räuber A 1977 *Appl. Phys.* **12** 355

Laguta V V, Glinchuk M D, Bykov I P, Karmazin A A, Grachev V G and Troitskii V V 1987 *Fiz. Tverd. Tela* **29** 2473 (Engl. Transl. 1987 *Sov. Phys.-Solid State* **29** 1422)

Malovichko G I and Grachev V G 1985 *Fiz. Tverd. Tela* **27** 2789 (Engl. Transl. 1985 *Sov. Phys.-Solid State* **27** 1678)

Malovichko G I, Grachev, V G and Lukin S N 1986 *Fiz. Tverd. Tela* **28** 991 (Engl.Transl. 1986 *Sov. Phys.-Solid State* **28** 553)

Niklas J R 1983 *Habilitationsschrift* Universität Paderborn

Peterson G E and Bridenbaugh P M 1968 *J. Chem. Phys.* **48** 3402

Peterson G E, Bridenbaugh P M and Green P 1967 *J. Chem. Phys.* **46** 4009

Peterson G E and Carnevale A 1972 *J. Chem. Phys.* **56** 4848

Peterson G E, Glass A M and Negran T J 1971 *Appl. Phys. Lett.* **19** 130

Petrov M P 1968 *Fiz. Tverd. Tela* **10** 3254 (Engl. Transl. 1968 *Sov. Phys.-Solid State* **10** 2574)

Phillips W, Amodei J J and Staebler D L 1972 *RCA Rev.* **33** 94

Räuber A 1978 *Current Topics in Material Science* vol 1, ed E Kaldis (Amsterdam: North-Holland) pp 481–601

Rexford D G and Kim Y M 1972 *J. Chem. Phys.* **57** 3094
Schempp E, Peterson G E and Carruthers J R 1970 *J. Chem. Phys.* **53** 306
Schmidt F and Voszka R 1981 *Cryst. Res. Technol.* **16** K127
Seidel H 1961 *Z. Phys.* **165** 218
—— 1966 *Habilitationsschrift* Universität Stuttgart
Seidel H and Wolf H C 1968 *Physics of Color Centers* ed W B Fowler (New York: Academic) pp 537–624
Smyth D M 1983 *Ferroelectrics* **50** 93
Söthe H, Rowan L G and Spaeth J-M 1989 *J. Phys.: Condens. Matter* **1** 3591
Takeda T, Watanabe A and Sugihara K 1968 *Phys. Lett.* **27A** 114
Terhune R W, Lambe J, Kikuchi C and Baker J 1961 *Phys. Rev.* **123** 1265
Zaldo C and Agulló-López F 1989 *Solid State Commun.* **71** 243